11

Magnetic Force Microscopy: Images of Nanostructures and Contrast Modeling

A. Thiaville, J. Miltat, and J.M. García

Magnetic force microscopy is a scanning technique, derived from atomic force microscopy, that maps the magnetic interaction between a sample and a magnetic tip. It is simple to use (most microscopes operate in ambient conditions) and provides images with a resolution down to 20 nm in best cases. The images do not, however, correspond directly to the sample magnetization, because of the long range of magnetic forces, their complex sources, as well as the potentially perturbing effect of tip-sample interaction. The emphasis of this chapter is on contrast modeling, especially in nanostructures.

11.1 Introduction: The Magnetic Force Microscope

The invention of scanning tunneling microscopy (STM, 1982) and subsequently of atomic force microscopy (AFM, 1986) caused a revolution in surface science. They enabled observation in real space of surface structures down to the atomic scale. In fact, a new generation of microscopes was born, the near-field scanning probe microscopes. Their key ingredients are:

- an actuator working at the atomic scale: this is the piezoelectric tube, where typically 1 V results in 1–10 nm displacements;
- a sharp tip whose apex can be brought in close proximity of the surface and interact with it, producing a signal that depends strongly on the tip-surface distance;
- a feedback system to control tip vertical position, owing to the detected signal and given a specific operating point (often called set point).

In STM, the signal is the tunnel current between tip and sample, both being conductive. It depends exponentially on the tip-sample distance, with a characteristic length of 0.1 nm. In AFM and a variety of derived techniques, the force between tip and sample is sensed by the deflection of a soft cantilever carrying the tip. The variety of techniques derived from the AFM expresses the variety of forces that can exist between tip and surface. Beside atomic forces (van der Waals, chemical interactions, etc.), electrostatic and magnetic forces are mainly detected. Thus, a magnetic force

microscope (MFM) is, simply speaking, an AFM in wich the tip can sense magnetic forces [1, 2]. Note that other scanning probe microscopes can be used for magnetic imaging without detecting forces. These are the scanning Hall probe microscope [3,4] and the scanning SQUID microscope [5, 6], where either the sample magnetic stray field or magnetic flux is measured inside a region with an area about one square micrometer. These techniques are covered in Chap. 13 of this book. The detection of a magnetic signal in an STM, using the spin-polarized tunnel effect, is covered in Chaps. 9 and 10.

Several reviews on MFM have already appeared. The first [7] is fairly representative of the status reached by the initial, homemade microscopes. The main modes of operation are well described, and many images on different samples are shown. The theory of MFM imaging in the regime of no perturbation is also discussed. The second [8] updates the apparatus description by presenting that of the current commercial machines. Imaging under an applied field is described in detail, with the demonstration of field effects on the tip, and specific examples of patterned elements imaging are shown. A recent encyclopedia article [9] is also helpful as a rapid introduction. Aside from these comprehensive texts, a number of papers with a review character appeared during the development of MFM [10–12]. Finally, some pages are devoted to MFM in the book on magnetic domains by Hubert and Schäfer [13]. Nevertheless, for the sake of legibility, the basis of MFM will be recalled briefly first. The core of the chapter will be devoted to the interpretation of MFM images and to their modeling. The emphasis will be laid on soft magnetic materials, i.e., those materials in wich the magnetic structures are dominated by magnetostatic energy (in contrast to hard materials in which the anisotropy energy dominates). Indeed, soft magnetic materials are more prone to perturbations by the MFM tip field and have been more resilient to observation by MFM. The following chapter, also devoted to MFM, proposes, on the other hand, a detailed discussion of the factors that determine the resolution of this microscope.

11.2 Principle of MFM

11.2.1 MFM Layout

The most common layout of an MFM is shown in Fig. 11.1 (atmospheric AFM operating in the vibrating mode). The piezo tube displaces the sample in the x and y directions in order to build, point by point, an image. The regulation couples deflection signals S, piezo z voltage, and tip vibration drive parameters A_d and ω_d. The signal at every point is derived from these three channels, as explained later. In fact, the various modes of AFM and MFM differ mainly in their regulation schemes.

The tip sits at the end of a flexible lever (called a cantilever), which is part of a larger chip that can be manipulated. Forces on the tip affect the position of the cantilever, whose instantaneous position is measured by reflection of a laser beam onto a position-sensitive detector. The cantilever is driven close to its resonance frequency by a piezo bimorph.

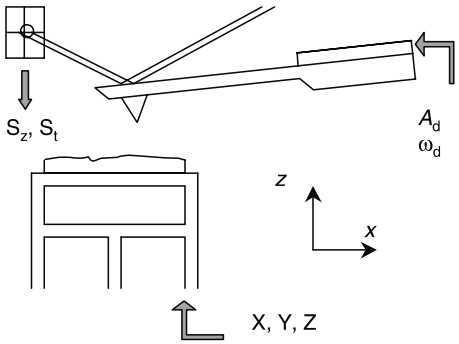

Fig. 11.1. Schematic of a MFM (vibrating mode). The various parts (piezo and sample, tip, tip chip, light detector) are not drawn on the same scale. The piezo tube moves the sample in x-, y-, z-directions under high voltages applied to separate electrodes. The small piezo bimorph, on which the tip chip is fixed, drives tip oscillations with amplitude A_d and angular frequency ω_d. The signal (cantilever deflection) is measured by the Poggendorf method: a laser beam is reflected onto a split photodiode. The difference of light intensity in the sectors gives access to tip vertical deflection (S_Z) or torsion (S_T)

Comments about the main parts of the microscope, in order to explain their specificity to MFM, appear worthwhile at this stage (see also Chap. 12 for instrumentation specific details):

1 A single piezo tube is used. This allows large sample displacements (more than 100 μm) if the tube is long enough, which is very convenient for magnetic structures as they involve different scales, from nanometers to tens of micrometers. Software aimed at correcting as much as possible the deficiencies of a piezo tube as an x-y actuator is actually required at large displacements.
2 Tips have evolved from etched magnetic wires to batch fabricated tip-cantilever chips prepared by micro-lithography [14], coated by a thin magnetic film. This ensures a great reduction of the tip stray field and tip magnetic volume, which favors a less invasive, higher resolution microscope operation. Additionally, the mechanical characteristics of the cantilevers are much better controlled. The usual cantilever materials are single crystalline silicon, or silicon nitride. Restoring force constants of the cantilevers span the $0.1 - 100\,\mathrm{Nm}^{-1}$ range, and resonance frequencies vary typically from 10 kHz to 1 MHz. The magnetic coating of the tip has a typical 5 – 50 nm thickness. It is often magnetically hard (large coercivity) so that the tip magnetic state is not changing during imaging. A very soft coating may, however, also be used for special purposes [15].
3 Cantilever motion is commonly measured by optical beam deflection [16], which is easy to adjust, flexible but space consuming. The other main technique, optical interferometry [17], is more compact and can be fitted inside the piezo tube in an arrangement where the tube carries the tip, so that one half-space is left for the sample and its environment (e.g., an electromagnet). Both techniques enable sub-angstrom motion detection.

11.2.2 Modes of Operation

While atomic forces are short-range (the van der Waals interaction energy between induced point dipoles falls off as $1/r^6$), magnetic forces are long-range (interaction between magnetic permanent dipoles falls as $1/r^3$). If magnetic contrast is to predominate, the tip has to fly at some distance from the surface. Experimentally, this distance is on the order of 10 – 100 nm. One of the reasons for the widespread use of MFM is its ability to image surfaces that are not flat on the nanometer scale. In that case, separation of magnetic forces from varying atomic forces due to topography requires some care. A simple procedure consists in measuring first the topographic profile for each scan line. By retracing the measured topography with an added vertical distance, the tip flies at a constant height above the surface. This is the "lift mode" introduced by Digital Instruments [18], and therefore, the tip flying height is sometimes also called the lift height. The magnetic signal is measured on the second pass, in which the topographic signal is close to constant if the lift height is large enough. Note that larger heights decrease tip stray fields, hence also the sample perturbation, but lead to lower signals and degraded resolution.

Two cases, therefore, need to be considered. The so-called no perturbation regime corresponds to tip and sample magnetizations that do not change when imaging is performed (rigid magnetizations). On the other hand, when the tip or sample magnetization changes during imaging, one speaks of perturbations. Section 11.5 is devoted to this second regime.

Another distinction, of an instrumental nature, separates operation modes in which the tip undergoes forced oscillations from those where it does not.

11.2.2.1 Static (DC) Mode

In this simplest mode, the force on the cantilever is measured by its instantaneous deflection. Under the assumption of rigid magnetization in tip and sample, the magnetic force on the tip is the gradient of the magnetostatic interaction energy

$$E_{\text{int}} = -\mu_0 \iiint_{\text{tip}} \vec{M}_{\text{tip}} \cdot \vec{H}_{\text{sam}} = -\mu_0 \iiint_{\text{sam}} \vec{M}_{\text{sam}} \cdot \vec{H}_{\text{tip}}. \tag{11.1}$$

Note the two equivalent formulations that exchange the roles of tip and sample (symbol: sam). The force components are thus

$$F_i = \mu_0 \iiint_{\text{tip}} \vec{M}_{\text{tip}} \cdot \frac{\partial \vec{H}_{\text{sam}}}{\partial x_i} = \mu_0 \iiint_{\text{sam}} \vec{M}_{\text{sam}} \cdot \frac{\partial \vec{H}_{\text{tip}}}{\partial x_i}. \tag{11.2}$$

This relation indicates that tips magnetized in different directions will be sensitive to the corresponding components of the stray field. This was verified for hard magnetic coatings [19]. As, due to the tip shape, the tip moment is stronger and more stable for axial magnetization, tips are most often magnetized along their axis. The cantilever deflection senses the force mainly in one direction, which is close to the normal of the sample surface (the cantilever is mounted with an inclination of about 10° so that

only the tip comes into contact). The lateral force produces a torsion of the cantilever. Torsion sensitivity is smaller than deflection sensitivity, roughly by the ratio of tip height to cantilever length (typically 10 over 200 μm). Thus, the main force is the vertical one, normal to the surface, F_Z. The minimal detectable force is limited by the thermal vibrations of the cantilever. With the usual spring constant $k = 1\ Nm^{-1}$, this force amounts to $\sim 10^{-11}$ N at room temperature [2].

11.2.2.2 Dynamic (AC) Modes

In this mode, the cantilever is driven close to resonance, and the gradient of the magnetic force comes into play. The description of the cantilever as harmonic oscillator, with quality factor Q and spring constant k, gives the following response to forced oscillations of amplitude A_d at an angular frequency ω_d [20]. The tip vertical position is $z = A\cos(\omega_d t + \varphi)$ with an amplitude

$$A = A_d\omega_r^2 \Big/ \sqrt{\left(\omega_r^2 - \omega_d^2\right)^2 + (\omega_r\omega_d/Q)^2} \tag{11.3}$$

and a phase

$$\varphi = \arctan\left(\omega_r\omega_d \Big/ \left[Q\left(\omega_r^2 - \omega_d^2\right)\right]\right). \tag{11.4}$$

To first order, the resonant angular frequency ω_r is related to the free oscillation value ω_0 and the gradient of the magnetic force by

$$\omega_r = \omega_0\sqrt{1 - (1/k)(\partial F_z/\partial z)} \sim \omega_0(1 - (1/2k)(\partial F_z/\partial z)). \tag{11.5}$$

Usual relative frequency shifts are small, on the order of 10^{-4}, justifying the expansion of the square root. In the same regime, where (11.1) is valid, the force gradient reads

$$\frac{\partial F_z}{\partial z} = \mu_0 \iiint_{\text{tip}} \vec{M}_{tip} \cdot \frac{\partial^2 \vec{H}_{\text{sam},z}}{\partial z^2} = \mu_0 \iiint_{\text{sam}} \vec{M}_{sam} \cdot \frac{\partial^2 \vec{M}_{\text{tip},z}}{\partial z^2}. \tag{11.6}$$

A positive force gradient produces a frequency decrease, usually coded black. As forces go to zero with increasing distance to the sample, a positive force gradient means that the tip is attracted toward the sample. For reasons of acquisition speed and insensitivity to external interferences, it has been recognized [20] that one should rather measure the cantilever oscillation (angular frequency ω_r, phase φ) than the amplitude A. As resonant frequencies are $10^4 - 10^5$ Hz and minimal detectable frequency shifts (due to thermal noise) are below 10^{-2} Hz, the force gradient limit is below 10^{-6} Nm^{-1}. For the sake of comparing with the static mode, consider a power-law variation of the magnetic force. One then has $\partial F/\partial z \propto F/z$, showing that at $z = 10$ nm a 10^{-6} Nm^{-1} gradient corresponds to a 10^{-14} N force, well below the static limit. This explains the popularity of the AC technique when compared to the DC mode. The comparison of both modes is also developed in Chap. 12, in terms of spatial resolution.

The finite quality factor Q results from friction in air and the interaction with the adsorbed water layer. It reaches about 100 in air and rises to 10^4–10^5 in vacuum [20, 21], but at the expense of ease of use. It is an important parameter because the minimum detectable frequency shift is again limited by thermal noise and is inversely proportional to the square root of Q.

The AC mode, disregarding amplitude detection, is split in two versions, wherein the signal is the phase (Eq. 11.4) or the frequency (Eq. 11.5). Phase imaging is simpler, as it requires only driving the cantilever at a constant frequency. However, one sees from Eq. 11.4 that this signal is a mixture of force gradient (through ω_r) and oscillation damping ($through Q$). The quality factor is not at all constant. As it depends mainly on hydrodynamic damping, it varies with tip height above the sample [22]. Therefore, the preferred AC mode is that in which the resonance frequency is tracked (through an additional feedback loop set at $\varphi = \pi/2$). Indeed, one sees from Eq. 11.4 that independently of Q, the condition $\varphi = \pi/2$ is reached when $\omega_d = \omega_r$. A recently developed AC mode takes advantage of the magnetic dependence of Q [23] to produce a magnetic dissipation image [24]. In the simplest arrangement with the frequency feedback operating, the resonance amplitude is $A = A_d Q$ so that the Q factor, and the dissipated energy, can be calculated from the measured A and ω_r [24]. Contrary to previous modes, a closed form expression for the dissipated power or the Q factor cannot be given. Indeed, many dissipation processes exist such as magneto-elastic coupling to phonons and eddy currents [25], irreversible wall motion, and damping of magnetization rotation [24].

11.3 Gallery of Nanostructures MFM Images

Nanostructures made out of soft magnetic materials, which are easily modified by applied fields if shape permits it, are nowadays the subject of intense research. Images demonstrating the MFM capabilities when applied to soft magnetic nanostructures are presented below.

11.3.1 Ultrathin Films

With ultrathin films, a sensitivity (in terms of a detectable magnetic moment) down to layers less than a nanometer thick, with domains as small as 200 nm, has been demonstrated. Figure 11.2 shows domains in cobalt films sandwiched by gold. Due to interface anisotropy, the magnetization stays perpendicular up to about 1.5 nm in thickness. The different contrasts correspond to up- and down-oriented domains, with respect to the (axial) tip magnetization direction. As the stable sample state is saturation, finite domains were produced by relaxation under fields slightly below coercivity. They have a ramified structure, the larger ones extending over several micrometers (see also Fig. 11.10, discussed later).

Domains in Cu/Ni/Cu ultrathin films were also observed with a magnetic thickness as small as 2 nm [28]. As shown below, ultrathin films are also interesting samples for studying the imaging process in the MFM.

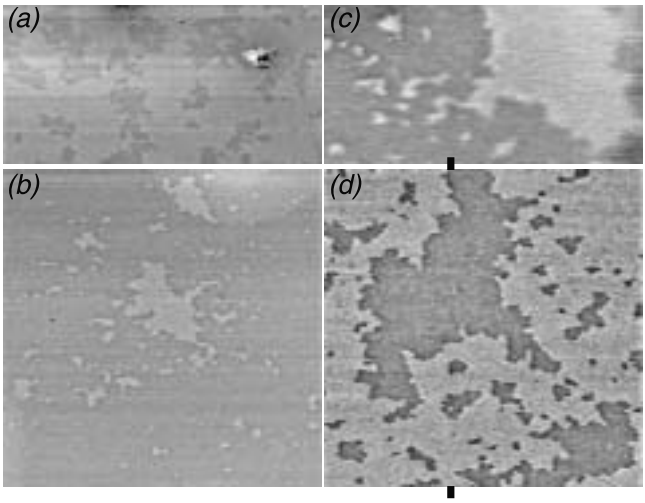

Fig. 11.2. Domains in Au/Co/Au films with ultrathin Co layers [26, 27]. Cobalt thickness is 6.2 Å **(a)**, 8.2 Å **(b)** and 13.9 Å **(c,d)**. Image widths are 30 μm **(a,b)** and 15 μm **(c,d)**. Images **(a,b,d)** were acquired with a tip covered with 200 nm CoCr, while the coverage was reduced to 50 nm in **(c)**. Lift height is 15 nm **(a,b,d)** and 20 nm **(c)**. Domains appear with a rather uniform contrast that increases, in comparison to noise, with cobalt thickness at constant tip coverage or with tip coverage at constant sample thickness

11.3.2 Nanoparticles

For samples where all dimensions are nanometric, MFM has also proved to be appropriate. Out of the many papers that appeared on this subject, Fig.11.3 displays

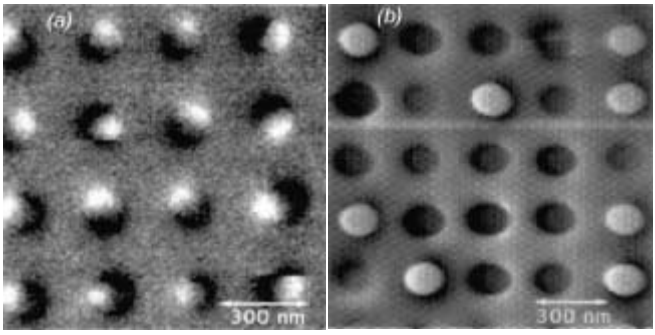

Fig. 11.3. MFM images of cobalt cylinders patterned by interference lithography [29]. Diameters are 100 nm **(a)**, 70 nm **(b)**, while heights are 40 nm **(a)**, 100 nm **(b)**. Shape anisotropy results in an in-plane **(a)** or out-of-plane magnetization **(b)**, with very different contrasts matching those expected from in-plane- and out-of-plane-oriented dipoles, respectively. Notice the switching of the bottom right particle in **(a)** during scanning

MFM images of patterned cobalt "nano-pillars" (where all dimensions are between 50 and 100 nm), with in-plane (a) and-out-of plane (b) easy-axis magnetization [29]. The contrasts (a) and (b) are very different, so that in both cases one can "see" the orientation of the magnetization in each particle.

Moreover, the individual switching of particles has been monitored, by performing imaging under an applied field [30]. With this tool, the static magnetic properties of each particle can be determined. As an example, thermally activated reversal in individual nanoparticles has been monitored with an MFM [31].

11.3.3 Nanowires

An extreme case of magnetic nanostructures is afforded by electrodeposited nanowires, where the diameter may be brought down to $\sim$ 35 nm while the length is as large as 20 μm. Observation of domain structures along such wires has been performed nearly exclusively by MFM, on wires deposited on a substrate [32, 33]. The detailed interpretation of the contrast becomes somewhat complex, as the tip does not at all move on a planar surface due to the wire topography. Consequently, as MFM does not directly sense the sample magnetization, it cannot be told from the images alone what the magnetization orientation in each part of the wire is, except in the case of single domain nanowires. This reveals one fundamental ambiguity of stray field imaging (see also Sect. 11.4.3).

11.3.4 Patterned Elements

An enormous wealth of magnetic structures is accessed when considering samples patterned out of a soft thin film, with lateral dimensions larger than the characteristic length of micromagnetics, so that they can sustain nonuniform structures [13].

As an example, systematic observations of the magnetic configuration as a function of the element size and aspect ratio (rectangular shape) were performed by R.D. Gomez [8, 34]. This allowed the classification of the possible domain structure in such elements (comparison with observations in the transmission electron microscope – Lorentz and Foucault modes, see Chaps. 4 and 5 – established that the

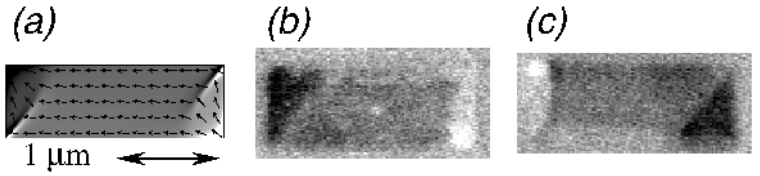

Fig. 11.4. A rectangular permalloy element (2.1 μm × 0.7 μm, thickness 16 nm) in the high remanence S state. **(a)** Calculated magnetic structure (2-D program, 5 nm mesh) with a gray-scale according to the magnetic charges (11.7). **(b,c)** MFM images for two opposite tip (axial) magnetizations (tip coverage 15 nm CoCr, lift height 20 nm). Note the variation in size of the end regions between **(b)** and **(c)**, due to tip-induced perturbations (see Fig. 11.16) [35]

structures were faithfully imaged). The contrasts pertaining to various types of walls (180°, 90° Néel walls, cross-tie wall, vortex) were also identified. Figure 11.4 shows two images of a rectangular NiFe element displaying a non-solenoidal configuration known as the S-state. Contrast is qualitatively similar to that of Fig. 11.3a, as the element is close to a single domain structure. However, due to its larger size, the charges at the ends are allowed to spread and form quasi-closure domain structures.

Figure 11.5 contains beautiful images of two cross-tie walls [36]. Adequate imaging conditions could only be obtained after the tip was demagnetized in order to gain a low moment, thus avoiding the perturbation of the structure. It is characterized as one 180° Néel wall, whose polarity alternates [13]. The transition regions are vortices ($S = +1$ circular Bloch lines) and cross lines ($S = -1$ Bloch lines), the latter at the origin of Néel walls of lower magnetization rotation angle extending perpendicular to the main wall.

Figure 11.6 shows the best observation, up until now, of vortex cores by MFM [37]. This observation was attempted by many people, but only recently met with success. One of the reasons is the small size of the vortex core. Indeed, micromagnetics shows that it extends over a few exchange lengths (5 nm for permalloy) [13]. Thus, a good resolution is necessary, as well as a low corrugation of the background. The absence of background signal requires circular edges of a good quality (otherwise small angle

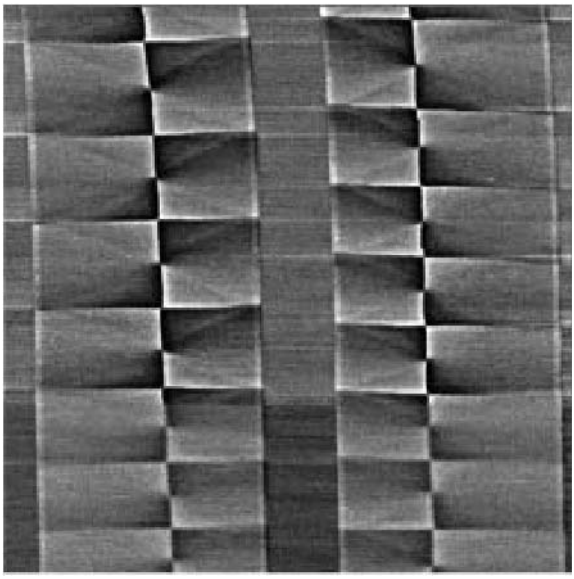

Fig. 11.5. Cross-tie walls in two 35-nm-thick, 12-μm-wide vertical NiFe strips [36], as imaged with a low moment, demagnetized tip (image size 30 μm). The secondary Néel walls perpendicular to the main wall extend to the strip edges, and contrast is distributed accordingly. With a standard Digital Instruments "MESP" tip, the central wall was displaced close to the strip edge and ripple-like structures were seen perpendicular to it, indicating a strong perturbation. Reprinted from [36] with permission from Elsevier Science

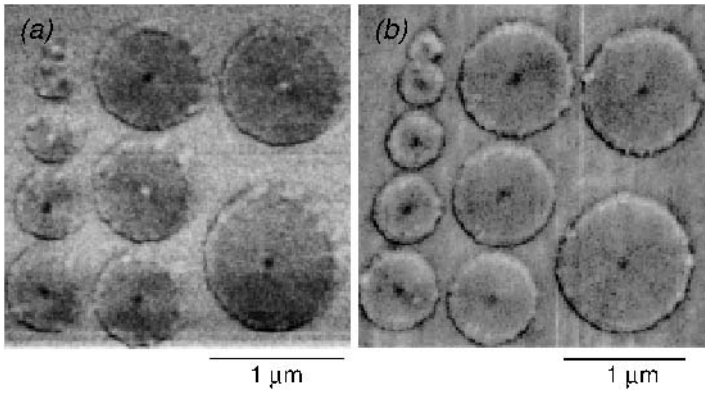

Fig. 11.6. Permalloy disks (thickness 50 nm) with diameters between 0.1 and 1 μm displaying the vortex structure [37]. After in-plane saturation at 1.5 T, different core orientations are seen **(a)**. After perpendicular saturation, all cores are aligned **(b)**. A "low-moment" CoCr-coated tip was used. The core contrast extends over about 50 nm. Reprinted with permission from [37]. Copyright American Association for the Advancement of Science

domain walls, or a diffuse contrast akin that in Fig. 11.4, is observed). Second, the tip should hardly displace the vortex during scanning, both in the magnetic attraction and repulsion regimes. This requires low tip fields, and small disk diameters that stabilize the vortex efficiently at the center.

11.4 MFM Contrast in Absence of Perturbations

This section examines the idealization of the MFM as a perfect measuring apparatus that does not change the state of the object while measuring it. This means that, although the tip applies a field to the sample, the reaction of the sample to this field will be neglected (see Sect. 11.5 for tip field evaluations). We also suppose that the tip is not affected by the sample field. Then, the only term of magnetic energy of the "sample + tip" system that changes with tip position is the interaction energy (11.1). Its derivatives with respect to tip height z give the force and force gradient. If one keeps in mind the idea of measuring the sample, these expressions are seen as integrals over tip volume of the sample stray field or its z-derivatives.

A first step in image interpretation is to assume that the tip is magnetically punctual. The natural model for a thin film-coated tip magnetized axially is that of a point monopole at the tip apex, with distributed monopoles of opposite sign at the bottom of the tip pyramid. Considering the large pyramid height, these remote monopoles are often disregarded. For a tip magnetized transverse to its axis, the point monopole approximation is insufficient and the point dipole model applies.

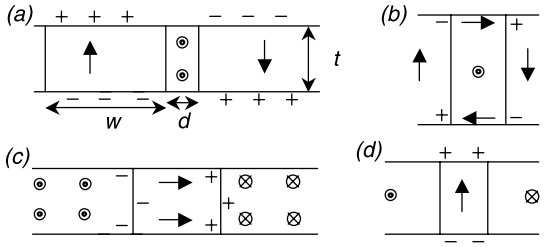

Fig. 11.7. Magnetic structures that enable 2-D stray field calculations. The film thickness has to be smaller than the exchange length in order to suppress magnetization variation across sample thickness. **(a)** A thin film with perpendicular anisotropy. The surfaces carry opposite charges. **(b)** Volume charges can appear on the walls if they transform to Néel wall, a process possible at thicknesses larger than the exchange length, or if the wall magnetization reverses at some places (presence of lines). **(c)** A thin film with easy-plane and planar magnetization. Volume charges exist around the Néel walls. **(d)** Surface charges appear when the magnetization is forced to become perpendicular, at vortex cores

11.4.1 Two-Dimensional Case

The evaluation of the stray field for an arbitrary magnetic structure has to be done numerically. However, in the case where the problem can be restricted to a two-dimensional one, analytical formulae can be obtained that are very helpful in understanding the results. The 2-D non-trivial situation is that of a (thin) film whose magnetic structure results in a 2-D charge distribution. For a magnetic structure, the magnetic poles (charge) density [13] consists of a volume term,

$$\rho = -div\,\vec{M} = -M_s\,div\,\vec{m}, \tag{11.7}$$

and a surface term (stands for the local surface normal, oriented outwards)

$$\sigma = \vec{M}\cdot\vec{n} = M_s\vec{m}\cdot\vec{n}. \tag{11.8}$$

The 2-D situation is realized for structures that do not vary across the film thickness, so that it is limited to thin film samples. This occurs in two main cases:

1. In films with perpendicular anisotropy, thin compared to the exchange length, walls are of pure Bloch-type, hence uncharged. One is left with only two opposite charge densities at the film surfaces (Fig. 11.7a). This case was considered in detail by H. Hug [28] in connection with experiments on ultrathin nickel films deposited on copper.
2. In films with in-plane magnetization that are thinner than the exchange length, a volume charge is present on both sides of the Néel walls (Fig. 11.7c).

In this case, the stray field is easily obtained in Fourier space. The transfer function approach that is appropriate for the description of the microscope in this regime is discussed in Chap. 12.

11.4.2 One-Dimensional Case

An even simpler situation is the 1-D case, in which fully analytical expressions of the stray field can be obtained. Such expressions are quite helpful in evaluating MFM contrast as a function of its parameters: film thickness t, tip flying height z, domain width w, and domain wall thickness d. The 1-D situation is that of a periodic domain structure, with parallel domain walls of infinite length (Fig. 11.7a).

Consider first a charge distribution at the sample top surface. For $z \neq 0$, the stray field reads

$$H_x = (1/2) M_s \sin(kx) \exp(-k|z|). \tag{11.9a}$$

$$H_z = (1/2) \operatorname{sign}(z) M_s \cos(kx) \exp(-k|z|). \tag{11.9b}$$

The stray field for a given structure is obtained by superposition of such expressions, via decomposition of the magnetization in a Fourier series $k = (2n+1)\pi/w$. As H in Eq. 11.9 is a complex exponential, the summation of the series is possible. In the case of perpendicular magnetization *with zero wall thickness*, one finds after some algebra

$$H_x = \frac{M_s}{\pi} \left[\operatorname{arctanh}\left(\frac{\sin(\pi x/w)}{\cosh(\pi z/w)} \right) - \operatorname{arctanh}\left(\frac{\sin(\pi x/w)}{\cosh(\pi(z+t)/w)} \right) \right], \tag{11.10}$$

$$H_z = \frac{M_s}{\pi} \left[\arctan\left(\frac{\cos(\pi x/w)}{sinh(\pi z/w)} \right) - \{z \to z+t\} \right], \tag{11.11}$$

$$\frac{\partial H_x}{\partial z} = -\frac{M_s}{w} \left[\frac{\sin(\pi x/w)\sinh(\pi z/w)}{\cosh^2(\pi z/w) - \sin^2(\pi x/w)} - \{z \to z+t\} \right], \tag{11.12}$$

$$\frac{\partial H_z}{\partial z} = -\frac{M_s}{w} \left[\frac{\cos(\pi x/w)\cosh(\pi z/w)}{\sinh^2(\pi z/w) - \cos^2(\pi x/w)} - \{z \to z+t\} \right], \tag{11.13}$$

These expressions have apparently not appeared in the literature yet. They are built as the difference of two contributions, arising from the opposite charge distributions at the two surfaces. This is indicated in the equations that follow Eq. 11.10, by the substitution rule $\{z \to z+t\}$; Eq. 11.10 being fully written.

A finite domain wall thickness may be modeled in a first approximation as a linearly varying surface charge located on the sample surfaces. Then, using the same procedure as above, one gets, for example,

$$\frac{\partial H_z}{\partial z} = \frac{M_s}{\pi d} \left[\operatorname{arctanh}\left(\frac{2\cosh(\pi z/w)\sin(\pi d/2w)\cos(\pi x/w)}{\sinh^2(\pi z/w) + \sin^2(\pi d/2w) + \cos^2(\pi x/w)} \right) - \{z \to z+t\} \right]. \tag{11.14}$$

Similar expressions can be constructed for the in-plane case with volume charges only. Indeed, the z derivative of the fields in the volume charge case is proportional

to the fields of the surface charge case. These expressions are however less useful, because 1-D domain structures are very rare for planar magnetization samples.

Finally, one should not forget that even in the no perturbation regime these expressions give the MFM contrast only for a point monopole or dipole tip. An integration over the tip is necessary in general.

One application of these analytical formulas concerns ultrathin films with perpendicular magnetization. In Fig. 11.8a, $\partial H_z/\partial z$ above a 1 nm film with 500-nm-wide domains is plotted at several tip heights $z = 10$, 50, and 100 nm (as explained in Sect. 11.5, this derivative is proportional to the frequency shift for a point monopole tip). At the low flying height, contrast is localized on the domain walls, and depends on domain wall thickness (the maximum signal (normalized to M_s) is $1.8 \times 10^{-3}\,\mathrm{nm}^{-1}$ for $d = 0$, and 1.0 at $d = 30\,\mathrm{nm}$). At large flying height, a domain-like contrast appears, which does not depend on d, as the latter is small compared to z. The intermediate case shows a contrast at domain center that is non-zero, but much smaller

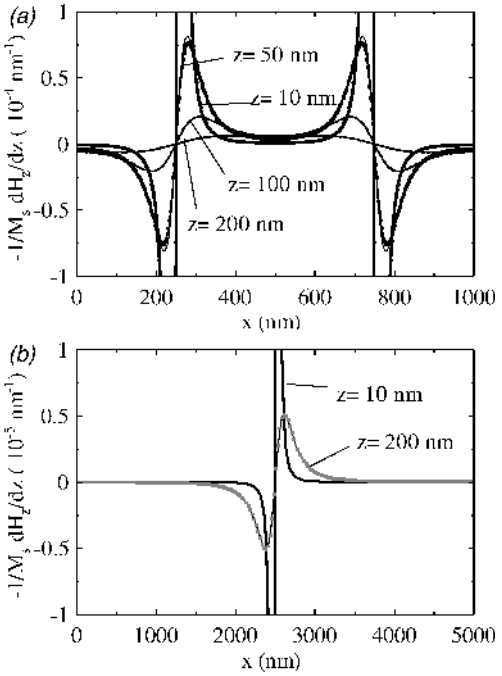

Fig. 11.8. Calculated MFM contrasts for a 1-D pattern, consisting of large domains in an ultrathin film 1 nm thick, with perpendicular magnetization. **(a)** Domain width $w = 500$ nm, tip flying height $z = 10$, 50, 100, and 200 nm, wall width $d = 0$ and 30 nm. **(b)** Domain width $w = 5{,}000$ nm, tip flying height $z = 10$ and 200 nm, wall width $d = 0$ and 30 nm. Domain contrast may appear at the smaller period, but completely vanishes for the large one, even if z is raised to 200 nm. The domain wall width of 30 nm has an influence only on the profiles with small flying heights (for example, in **(a)** at $z = 50$ nm, the thin curve is for $d = 0$ nm, while the thick one with symbols is for $d = 30$ nm)

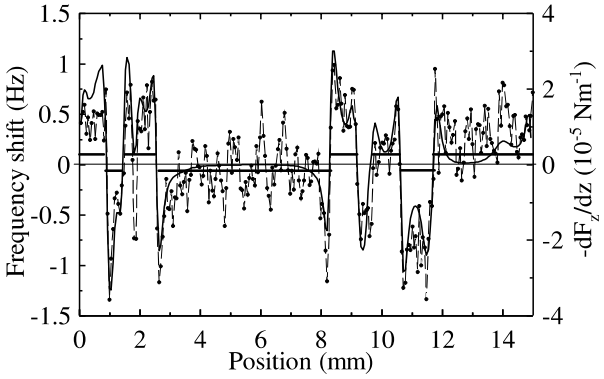

Fig. 11.9. Experimental line profile (dots) from Fig. 11.2d, and corresponding profile calculated for a point monopole tip using the 2-D approach. The data are averaged over five columns of the image, indicated by markers on Fig. 11.2d (the whole image contains 256 lines). The average contrasts measured on 20×20 pixels boxes, five for each contrast, placed in large areas of uniform contrast, are also indicated (thick broken horizontal lines; the variance on these values is 0.13 Hz). The calculation corresponds to a point monopole located at 180 nm above the sample that creates a maximum induction at sample level of 56 mT (field 45 kA m^{-1})

(1/20) than the maximum contrast at the domain walls. For $z = 200$ nm, the contrast maximum moves to the domain center. Such calculations cast some light on the puzzling observation of domain-like contrast in ultrathin films with perpendicular magnetization (Fig. 11.2). Indeed, as the films are ultrathin, the stray field is almost entirely concentrated inside the film. Outside, it should exist only above the domain walls. These exact calculations show that at large flying heights contrast can appear inside the domains if they are not too large (compare Fig. 11.8a and b). Nevertheless, if real images have to be fitted, the 2-D approach is necessary.

Figure 11.9 shows a line scan of Fig. 11.2, compared to a calculation for a point monopole tip located at 180 nm from the surface. The 2-D calculation was performed on a domain structure obtained by assigning dark and light pixels in Fig. 11.2d to up- and down-oriented domains with zero wall thickness (as first done by Hug [28]). The experimental trace is well reproduced, given the noise of the image. However, this recessed monopole position may appear too large, even for a 200 nm tip-coating thickness. Also, the average domain contrasts are still larger than those calculated (but their difference is on the order of statistical noise). This called for more precise experiments.

Figure 11.10 is a large scale image (60 μm) of a region with a square domain of 40 μm size. The domain was "written" on the saturated layer by MFM with a tip having a thick coating ($Co_{80}Cr_{20}$ alloy, 30 nm) that produces a large stray field. The sample is a cobalt ultrathin film (1.4 nm) sandwiched by platinum (see [38] for a general presentation of the sample properties). Imaging was performed with a tip covered by sputtering half the "writing" thickness, actually the same value used for imaging patterned permalloy elements (see Sect. 11.5.3). The very straight domain

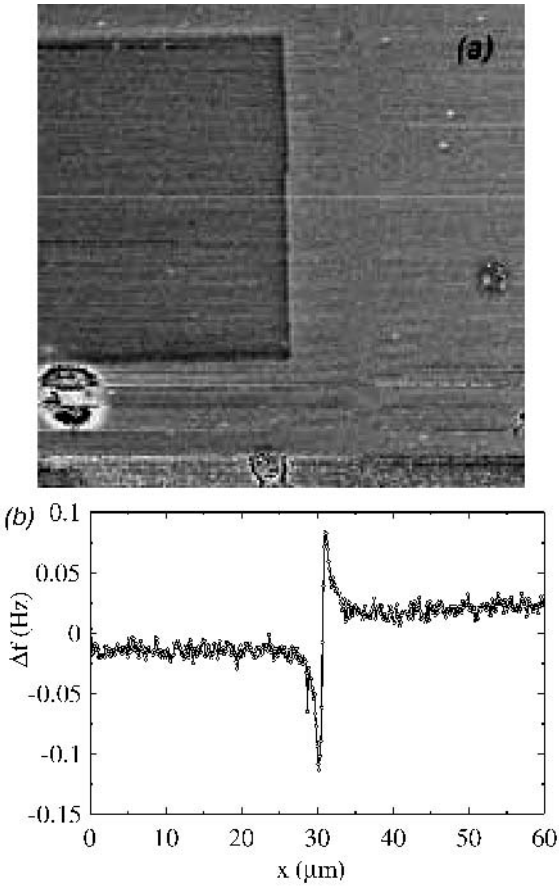

Fig. 11.10. MFM image of a 40 μm square domain in a Pt/Co(1.4 nm)/Pt ultrathin film **(a)**. The domain was "written" first by imaging several times this square with a tip having a thick magnetic coverage. The image is 60 μm in size, and the tip lift height is 25 nm. A contrast profile **(b)** obtained by averaging over 150 lines (the image contains 512 lines) shows, on top of a domain wall contrast (0.2 Hz), a domain contrast tens of micrometers away from the wall (0.03 Hz)

wall (Fig. 11.10a) allows for an averaging over many line profiles. As a result, a small but clear contrast can be seen very far (tens of micrometers away) from the wall (Fig. 11.10b). If this data is compared to Eq. 11.14 at an infinite domain width, the contrast step between the two domains cannot be reproduced. This definitely calls for further investigation of MFM imaging of ultrathin films.

The formulas above are also helpful in the discussion of MFM spatial resolution. Even if the probe is as small as a point-like magnetic structure (monopole, dipole), the tip flying height profoundly affects the images. This is exemplified in Fig. 11.11, drawn for parameters appropriate to FePd ordered alloys films. These samples have

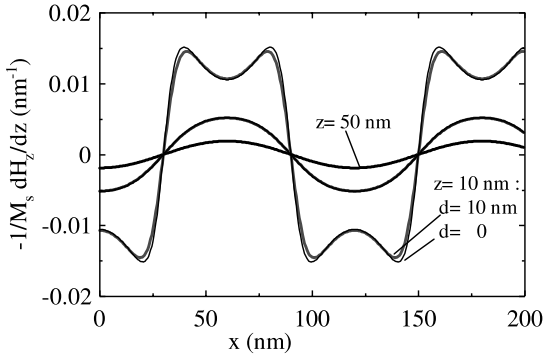

Fig. 11.11. Calculated MFM contrasts for a 1-D pattern with fine domains. Parameters are those of FePd films ($t = 30$ nm, $w = 60$ nm, $d = 10$ nm). Flying heights $z = 10$, 30, and 50 nm are compared. Only at the smallest value can one say that the structure is really resolved (the curve with zero domain wall width differs from that at $d = 10$ nm)

shown the smallest regular domains (of width 60 nm) up until now [39]. One sees that usual flying heights only give sinusoidal contrast profiles, because they are too large compared to the domain width.

11.4.3 MFM as a Charge Microscopy

It was recognized early [19] that the MFM images of soft elements with in-plane magnetization were similar to those of the magnetic charge distribution. This is vividly illustrated here by Figs. 11.3a and 11.4, where the charges considered are volume charges (11.7). For samples with perpendicular magnetization, the similarity is also apparent if one considers the surface charges (11.8) on the upper sample surface (Figs. 11.2, 11.3b). As the magnetic charges are the sources of the stray field (there is no stray field if they are zero everywhere), it is also quite natural to see the MFM images as charge pictures. This conception was formalized by A. Hubert and coworkers [40]. The interaction energy (11.1), considering its second form in which integration is performed over the sample, can be rewritten with the help of the magnetostatic potential ϕ_{tip} from which the tip field derives ($\vec{H}_{\text{tip}} = -\vec{\nabla}\phi_{\text{tip}}$) as an integral over the volume and surface charge densities

$$E_{\text{int}} = \mu_0 \iiint_{\text{sam}} \rho\phi_{\text{tip}} + \mu_0 \iint_{\text{sam}} \sigma\phi_{\text{tip}}. \tag{11.15}$$

We have thus alternative expressions of the force, in terms of magnetic charges

$$\begin{aligned} F_z &= \mu_0 \iiint_{\text{sam}} \rho_{\text{sam}} H_{\text{tip},z} + \mu_0 \iint_{\text{sam}} \sigma_{\text{sam}} H_{\text{tip},z} \\ &= \mu_0 \iiint_{\text{tip}} \rho_{\text{tip}} H_{\text{sam},z} + \mu_0 \iint_{\text{tip}} \sigma_{\text{tip}} H_{\text{sam},z}. \end{aligned} \tag{11.16}$$

An interpretation of these expressions is that the suitable derivative of the tip potential is the response function of the charge microscope: Its magnitude determines the signal, its localization sets the resolution. Profiles of the potential and its derivatives were computed in [40] for various tip shapes: They roughly extend over the thickness of the tip coating, when the flying height is below this thickness. These profiles were obtained under a specific assumption about the tip magnetic structure, but it can be accepted that for any tip such a more or less localized potential will exist. Potential profiles were also determined experimentally from the analysis of images on point-source like magnetic objects [41].

This conception of MFM is rather efficient for a quick survey of the images. For a more thorough understanding, however, a number of difficulties arise. Consider for example the ultrathin film case discussed before (Figs. 11.2, 11.9). In the domains, one has two equal and opposite charge densities at the surfaces, spaced 1 nm apart. Thus, seen from a distance of tens to hundreds of nanometers, it is meaningless to assume that the top surface charge determines the contrast. These two opposite charge densities just cancel, and contrast should only remain in the vicinity of domain walls. Figure 11.8a was drawn for periodic stripe domains of width $w = 500$ nm. For a width 10 times larger, the contrast becomes clearly localized at the walls (Fig. 11.8b). The charge picture is here inadequate: It leads to the expectation of a domain contrast that converges to a constant non-zero value at infinite distance from domain walls, which is not found by exact calculations. And if one just reduces the film to a purely 2-D structure, all charges disappear (walls are Bloch walls, i.e., the divergence of magnetization is zero) and no force signal is expected.

A second example is afforded by the vortex structure. As schematically drawn in Fig. 11.7d, it features a perpendicularly magnetized core at the center of a circularly rotating in-plane magnetization pattern. A strictly in-plane vortex would bear no charge (it is a flux closure structure), and the center magnetization would be zero. Due to the exchange interaction, a real vortex has a finite width core with perpendicular magnetization. The surface charges of the core are conducive to a deviation of the magnetization from the circular rotation, so that both volume and surface charges occur. They are drawn in Fig. 11.12, together with the magnetization. The charge pattern is complex, as volume charges opposite to surface charges extend below the latter. The resulting contrast is not easy to figure out. The partial compensation of surface by volume charges may explain why vortex core observations by MFM are so rare. One can anticipate that this will be possible only in a certain range of thickness. In that case, as the structure is not as simple as the idealization, the charge pattern is complex and in some respect unknown. The rather wide contrasts in Figs. 11.4 and 11.5 testify to the ability of charges to spread out. Thus, for a given sample the precise charge distribution should be computed. Then, the effort is not much larger if one computes the stray field simultaneously.

A final remark should be made about the inversion problem (i.e., given an MFM image, find the magnetic structure). It has been proved that the information supplied by the MFM is not sufficient for this purpose [43]. A simpler inverse problem, namely, the recovery of the magnetic charges distribution, was also proved to be hopeless [44]. In fact, surface and volume charges play equivalent roles. In the case of films, MFM

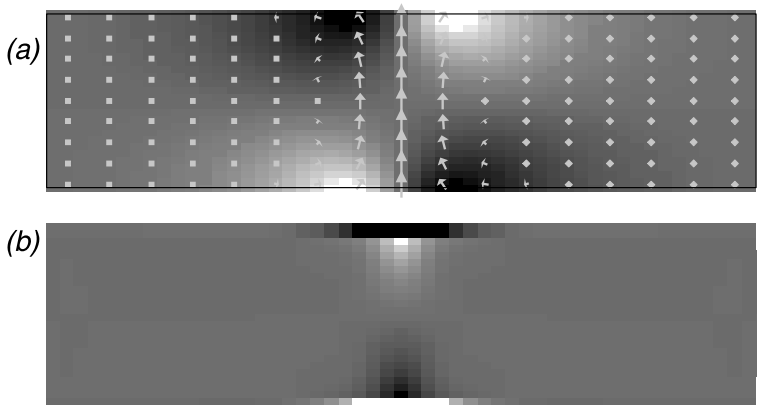

Fig. 11.12. Numerically computed 3-D structure of a vortex in a 200 nm diameter, 50-nm-thick permalloy disk, with a mesh size of $4 \times 4 \times 2$ nm. The structures are displayed in a vertical cross section that contains the disk axis. The magnetization pattern **(a)** was coded in gray scale according to the radial component, whose presence means that the divergence-free situation is not realized. The magnetic charges (sum of volume and surface contributions for the surface cells) are drawn in **(b)** with a gray scale representation. Volume charges are seen to be opposite to the nearest surface charges linked to the core magnetization of the vortex. Computations were performed with the OOMMF software [42]

images can always be related to equivalent surface charges (effective charges [44]). Thus, an external source of knowledge is always necessary in order to interpret MFM images.

11.5 MFM Contrast in the Presence of Perturbations

It was recognized early that, for soft samples, the MFM image of the magnetic structure may appear strongly distorted [45]. The replacement of etched wires by thin-film coated tips led to a great reduction of tip stray fields and allowed for much more faithful images. Nevertheless, complete avoidance of tip stray field is not the solution, as from Eq. 11.1 no contrast would then exist. Therefore, one has to accept the presence of this field. Ideally, it would be tailored so as to give, for the sample considered, the lowest detectable contrast. More sensitive microscopes are thus still needed.

11.5.1 Tip Stray Field Values

Several experiments have been devised to measure the tip stray field magnitude and spatial distribution. The most direct determination was obtained by measuring the deflection of high energy electrons passing close to the tip in a STEM [46], see Chap. 4. A typical value for Digital Instruments standard “MESP” probes is a maximum axial

induction of 40 mT (field of 32 kA m^{-1}) at about 50 nm from the tip apex, the lateral FWHM being 0.25 μm. A more indirect technique involved deconvoluting maps of Hall voltage versus tip position, using micron-size Hall sensors [47]. Maximum values were found to be 10 – 20 mT (8 – 16 kA m^{-1}) at 100 nm from the tip apex.

Additionally, the tip stray field can be fitted to experimental data, provided the sample structure is well known. Such is the case of ultrathin Ni layers (10 nm) on Cu, with perpendicular magnetization, narrow Bloch walls and large domains [48]. Fields determined for tips covered with about 10 nm of iron by evaporation had maximal values at apex of 10 mT (8 kA m^{-1}) and a FWHM less than 0.1 μm.

Whatever the exact result of these measurements, the values found are not small for soft samples when compared to coercive fields on the order of 100 A m^{-1} (in-plane) and anisotropy fields on the order of 1 kA m^{-1} (in-plane). However, tip fields are sharply localized, and their effect cannot be guessed from that of an equivalent uniform field. In recent years, micromagnetic calculations have been applied to this problem. In some cases, results could be compared in detail to experiments, as shown below.

11.5.2 Forces in the Case of Perturbation

This discussion is restricted first to the case where the tip magnetic structure remains unaffected. This approximation is reasonable for the experimental configuration of a magnetically hard tip and a soft sample. The total magnetic energy, dropping the constant tip internal energy, is now

$$E_{\mathrm{mag}} = E_{\mathrm{int}} + E_{\mathrm{sam}}, \tag{11.17}$$

where the interaction term is Eq. 11.1. In the frame of micromagnetics [13], the local sample magnetization has a constant magnitude M_s and a direction vector (unit vector). The two contributions, therefore, read

$$E_{\mathrm{int}} = -\mu_0 M_s \iiint_{\mathrm{sam}} \vec{m} \cdot \vec{H}_{\mathrm{tip}}, \tag{11.18}$$

$$E_{\mathrm{sam}} = \iiint_{\mathrm{sam}} A\left(\nabla \vec{m}\right)^2 + KG\left(\vec{m}\right) - (\mu_0 M_s/2)\vec{m} \cdot \vec{H}_{\mathrm{sam}}. \tag{11.19}$$

The energy contributions to the sample energy are called exchange, anisotropy, and magnetostatic energies, respectively.

Here arises an essential question: Which energy should one consider in order to evaluate the magnetic force on the tip? It has sometimes been assumed ([49], for example) that the sole interaction energy (Eq. 11.1) is appropriate, and, in fact, a direct extension of the no perturbation case. Let us consider the question at a basic level. As there are no forces other than magnetic and elastic, the "sample + tip-cantilever" system is isolated and its energy is constant. Therefore, the tip moves under the gradient of the total magnetic energy. In the case of no perturbation (no change of the sample and tip magnetization configurations), the sample and tip energies do not

change, so the force results from the sole interaction term. This is, however, no longer true if the sample magnetization is allowed to change.

Typical MFM tips, because of their mechanical softness, vibrate at frequencies below 100 kHz. These are low compared to natural frequencies of magnetic structures, which are on the order of GHz [50]. Therefore, a first approximation is to consider the quasi-static limit of the problem: At each tip position (in x, y, and z) the sample magnetization is allowed to reach equilibrium by minimizing E_{mag} with respect to $\vec{m}$. This calculation is just what micromagnetic codes can perform.

The force on the tip is the sum of an external contribution (the tip field at sample level varies with tip height) and of an induced contribution, as the sample magnetization reacts to tip field. Therefore, we write the total derivative (symbol d) with respect to the tip height as the sum of the partial derivative (derivative over the terms that explicitly contain z_{tip}, symbol ∂) and the "motion" term (through the variation of the equilibrium magnetization with tip height)

$$F_z = -\frac{dE_{\mathrm{mag}}}{dz_{\mathrm{tip}}} = -\frac{\partial E_{\mathrm{mag}}}{\partial z_{\mathrm{tip}}} - \frac{\delta E_{\mathrm{mag}}}{\delta \vec{m}} \cdot \frac{D\vec{m}}{Dz_{\mathrm{tip}}}. \tag{11.20}$$

For the variation of the energy with the magnetization, we use the functional derivative symbol (δ) customary to functionals that involve the gradient of the variable [13]. The evolution of the sample magnetization with tip height is denoted by yet another symbol, D. As we assumed that the sample magnetization is in equilibrium at every position of the tip, the energy is stationary with respect to variations of $\vec{m}$ (i.e., $\iiint (\delta E_{\mathrm{mag}}/\delta \vec{m}) \cdot \Delta\vec{m} = 0$ for any variation $\Delta\vec{m}$ of the magnetization), so that one is left with the explicit term, which reads

$$F_z = \mu_0 M_s \iiint_{\mathrm{sam}} \vec{m} \cdot \frac{\partial \vec{H}_{\mathrm{tip}}}{\partial z_{\mathrm{tip}}}. \tag{11.21}$$

In this expression, the magnetization distribution $\vec{m}$ is that which is at equilibrium under the tip field associated with the tip position considered; it is generally different from the magnetization in the absence of the tip field, denoted by $\vec{m}$. Note that if we had evaluated the gradient of the interaction energy (Eq. 11.1), since $\iiint (\delta E_{\mathrm{int}}/\delta \vec{m}) \cdot \Delta\vec{m} \neq 0$, an additional term would be present in the integral (namely, $\vec{H}_{\mathrm{tip}} \cdot D\vec{m}/Dz_{\mathrm{tip}}$). It is now important to understand that Eq. 11.21 remains the same when the tip magnetization distribution is also changing due to perturbation, again because of stationary conditions. One *only* has to use the modified tip field, not that of the tip without the sample.

Turning now to the dynamic mode, we calculate the force gradient from the force (11.21). Here, nothing cancels out, and one obtains

$$\frac{dF_z}{dz_{\mathrm{tip}}} = \mu_0 M_s \iiint_{\mathrm{sam}} \frac{D\vec{m}}{Dz_{\mathrm{tip}}} \cdot \frac{\partial \vec{H}_{\mathrm{tip}}}{\partial z_{\mathrm{tip}}} + \vec{m} \cdot \frac{\partial^2 \vec{H}_{\mathrm{tip}}}{\partial z_{\mathrm{tip}}^2}. \tag{11.22}$$

A third term should be added in the general case to express the modification of the tip field due to tip position-dependent perturbation.

The literature contains many experimental demonstrations of the existence of perturbations, even for the standard tips used nowadays. Trivial cases are those where the structure changes during scanning (see, e.g., Fig. 11.3a bottom right corner dot), or grossly differs from what is known, either by another technique or by our knowledge of magnetic structures. These cases can sometimes be avoided by using low moment tips and large flying heights. More subtle perturbations, which only change the details of the image, also exist. A check consists of reversing tip magnetization (see Figs. 11.4 and 11.13). From Eq. 11.21, one can express the sum of two images with opposite tip magnetizations as

$$F_z(+) + F_z(-) = \mu_0 M_s \iiint_{\text{sam}} \frac{\partial \vec{H}_{\text{tip}}(+)}{\partial z_{\text{tip}}} \cdot \left[\vec{m}\,(+) - \vec{m}\,(-)\right]. \tag{11.23}$$

If the magnetization is unperturbed, $\vec{m}(+) = \vec{m}(-) = \vec{m}_0$ and the result is zero. Otherwise, there is some perturbation. Obviously, the tip has to be reversed many times so as to check for reproducibility of its structure. This approach was first used in [51, 52].

11.5.3 Perturbations in Patterned Permalloy Elements

Figure 11.13 shows the structure of a 2 μm permalloy square exhibiting the flux-closure structure with four domains. The MFM images correspond well to this schematic pattern, however, with a small deformation. Comparing the 2 images taken with opposite tip magnetizations, a curvature of the domain walls is apparent.

Another feature of the images is the global attractive force (negative frequency shift) when the tip is above the element, with respect to the tip above the nonmagnetic substrate. This attraction is present irrespective of tip magnetization. A mechanism for tip attraction was put forward by J.J. Saenz [53] in the case of perpendicularly magnetized samples. It may, however, be generalized. A magnetic material (except when saturated in the direction of the field) has a non-zero susceptibility χ. Idealizing

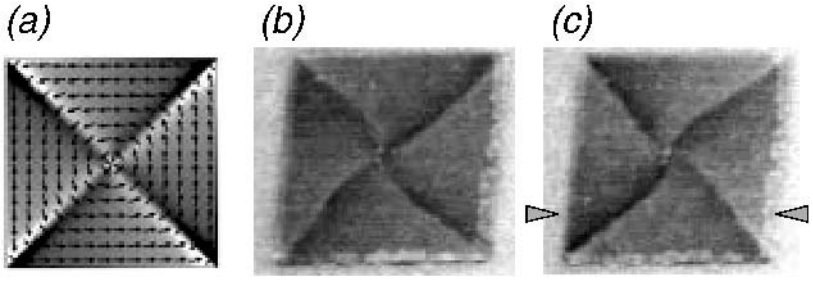

Fig. 11.13. Images of a 16-nm-thick permalloy square with 2 μm edge length: **(a)** calculated structure in zero field, with gray scale shading according to the magnetic charge (mesh 5 × 5 × 16 nm); **(b,c)** MFM images with opposite tip polarities (tip coating 20 nm CoCr, lift height 20 nm)

it by a paramagnet, one gets $E_{\mathrm{mag}} = -\mu_0 \chi (\vec{H}_{\mathrm{tip}})^2/2$, which gives rise to tip attraction. How this mechanism applies locally for a nonuniform magnetization distribution and in an inhomogeneous tip field has to be studied by micromagnetic calculations.

The occurrence of apparent wall curving is also best studied by such calculations. A 2-D micromagnetic program developed earlier (see [54,55] and references therein) was modified to include a tip field in wich the tip can be located at any position [56]. As a first approximation, the field of an effective monopole was used. In order to find the parameters (pole strength and vertical position) of the effective monopole, a finite elements micromagnetic calculation of a 3-D typical tip was performed [56, 57]. For each distance of a sample plane to the tip apex, the computed field profile was found to be close to that of a monopole. The monopole is only an approximation, however, as the fitted pole strength and position were found to vary systematically with distance to the tip apex [57], such that the effective monopole has a higher strength and is located farther inside the tip as the sample plane recesses from the tip apex. The calculated effect of the tip field on the sample micromagnetic structure is shown in Fig. 11.14 for several positions of the tip and both tip polarities. When the tip is above one domain (Fig. 11.14a,d), one sees clearly the appearance of an induced charge in the sample. This charge is opposite to that of the tip monopole

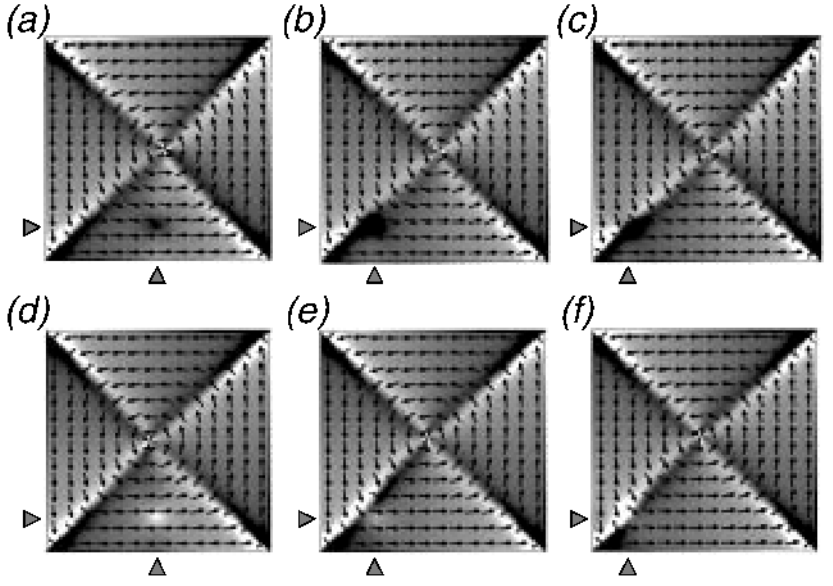

Fig. 11.14. Magnetization patterns of a square permalloy element exposed to the field of a negative (**a**–**c**) and positive (**d**–**f**) monopole tip. Gray-scale coding relates to the volume charge (this is a 2-D calculation). The monopole position is indicated by arrows. The sample is 1000 nm wide, 16 nm thick, and the mesh size is $4 \times 4 \times 16$ nm. The effective monopole of the tip is located at 60 nm from the top surface and creates a maximum axial field of 32 kA m^{-1} (induction 40 mT) in the film center. The induced charge is clearly seen, as well as its interaction with the wall charges

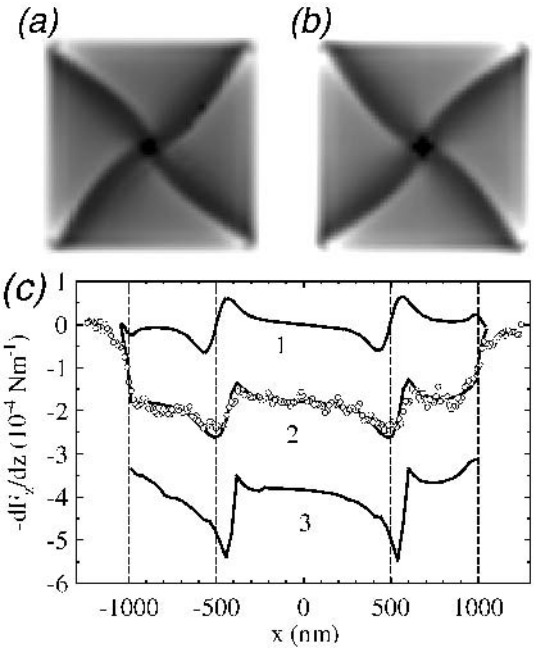

Fig. 11.15. Contrast calculations corresponding to the experimental results of Fig. 11.13. Calculated images **(a,b)** for a 1000-nm-wide, 10-nm-thick sample (home-developed 2-D program, mesh size $32 \times 32 \times 10$ nm), monopole tip at 60 nm from sample mid-plane, creating a maximum field of 32 kA m^{-1} (induction 40 mT). The gray scale encoding is such that black corresponds to a positive force gradient, as in the experiments. Note that the mesh size does not allow one to compute the vortex core, and that it is a 2-D calculation, so a contrast due to vortex core cannot appear. For the true sample size, **(c)** shows a line profile (dots) from Fig. 11.13c (markers) superposed with calculation results for this line. The calculation uses a sample 2000 nm wide, 16 nm thick (mesh size $16 \times 16 \times 16$ nm) and a monopole tip at 53 nm from sample mid-plane, creating at sample level a maximum field of 24 kA m^{-1}. The three lines are (1) no perturbation model; (2) calculations according to Eq. 11.22; (3) calculation of the force as the gradient of the interaction energy. The outer dashed lines indicate the sample edges, the inner dotted lines point to the wall positions in zero field. Frequency shifts were converted into force gradients using a cantilever stiffness $k = 5.2$ Nm^{-1}

and can be viewed as the image charge of the tip monopole in an imperfect shield (the permalloy sample). When the tip moves toward the walls, the induced charge follows and interacts with the wall structure. As the walls are of Néel type, they bear two opposite charge sheets on their sides. Thus, the tip in the top figures always pushes down the left wall to the left, while the opposite tip (bottom figures) pushes it to the right. This explains the characteristic wall deformation in the MFM images. Figure 11.15a,b display computed images (force gradient) for a 1 μm square; a very good qualitative agreement is found with the experiment. Figure 11.15c provides a quantitative comparison for the 2 μm square, for one scan line. The monopole

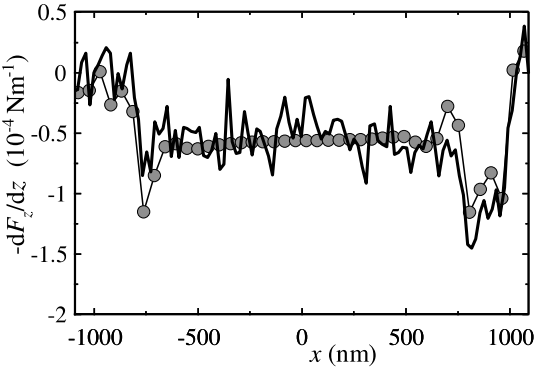

Fig. 11.16. Profile along the center line of Fig. 11.4 superposed to numerical simulation results. Calculation parameters are: mesh size $28 \times 28 \times 16$ nm, monopole tip at 53 nm from sample mid-plane, creating a maximum field of 11.1 kA m^{-1}, cantilever stiffness $k = 6.5$ Nm^{-1}

strength was slightly adjusted for a best fit. The global attractive force is clearly seen both in experiments and calculations. Wall position in the images is also correctly reproduced, as well as wall contrast. Note that the calculation, taking into account only the interaction energy, would predict twice the overall contrast and sharper walls (curve labeled 3).

Another calculation was performed for the rectangular element shown in Fig. 11.4. The phenomena are similar, and perturbation is visible as unequal sizes of the two quasi-closure domains at the ends. Figure 11.16 shows contrast profiles (experimental and calculated) along the central scan line, again with a nice agreement.

One should not deduce from the previous examples that all perturbation processes are best discussed in terms of induced charges. In other cases, thinking simply of the effect of the tip field on the sample magnetization is more direct. This is adequate, for example, in a rectangle with four domains and one vortex on the central wall when focusing on vortex motion [58].

Summarizing, it appears that micromagnetic calculations can, in some cases, reproduce MFM images in the presence of perturbations with a high accuracy. They also give insight into what happens in the sample during observation. For soft samples, the calculations show that the charge density in the sample can rearrange under tip fields, which calls for caution when considering the MFM as a microscope that "just maps" the sample charges.

11.6 Conclusion and Perspectives

Magnetic force microscopy has now become a standard magnetic microscope, operating in conditions similar to optical microscopes, but with a more than ten times better resolution. However, the signal is not related in a simple way to the magnetization direction in the sample just below the tip apex. Because magnetic forces are long

range, the signal contains a contribution from regions far from the tip. Moreover, such a signal is related to magnetic charges, rather than to the magnetization itself.

We have seen in this chapter that, in most cases, a qualitative image interpretation is readily obtained. But quantitative values, fine details, or even magnetization orientation in complex cases can remain obscure. Micromagnetic calculations of the sample have been shown to help in this respect, although one is still far from a complete modeling of the microscope.

Advanced magnetic force microscopes are still possible. Tips should be improved so that their magnetic structure is better controlled and their stray field strength tailored to each sample. More sensitive force detection schemes will allow for lower tip fields, hence lower sample perturbation and more faithful images. Finally, new contrast modes are continuously appearing, enriching the capabilities of this versatile microscope (for example see [59, 60]).

Acknowledgement. This chapter could not have been written without the work of Laurent Belliard [26] and Dalibor Tomáš [54] for their Ph.D., and of Denis Bourgeois for his masters theses. The work of JMG at Orsay was supported by an individual Marie Curie fellowship from the E.C.

References

1. Y. Martin and H.K. Wickramasinghe, Appl. Phys. Lett. **50**, 1455 (1987).
2. J.J. Saenz, N. Garcia, P. Gruetter, E. Meyer, H. Heinzelmann, R. Wisendanger, L. Rosenthaler, H.R. Hidber, and H.J. Guentherodt, J. Appl. Phys. **62**, 4293 (1987).
3. A.M. Chang, H.D. Hallen, L. Harriott, H.F. Hess, H.L. Kao, J. Kwo, R.E. Miller, R. Wolfe, J. van der Ziel, and T.Y. Chang, Appl. Phys. Lett. **61**, 1974 (1992).
4. A. Oral, S.J. Bending, and M. Henini, J. Vac. Sci. Technol. **B14**, 1202 (1996).
5. J.R. Kirtley, M.B. Ketchen, K.G. Stawiasz, J.Z. Sun, W.J. Gallagher, S.H. Blanton, and S.J. Wind, Appl. Phys. Lett. **66**, 1138 (1995).
6. J.R. Kirtley, M.B. Ketchen, C.C. Tsuei, J.Z. Sun, W.J. Gallagher, L.S. Yu-Jahnes, A. Gupta, K.G. Stawiasz, and S.J. Wind, IBM J. Res. Develop. **39**, 655 (1995).
7. P. Gruetter, H.J. Mamin, and D. Rugar, in *Scanning Tunneling Microscopy II*, edited by R. Wiesendanger and H.J. Guentherodt (Springer Verlag, Berlin, 1992).
8. R.D. Gomez, in *Magnetic Imaging and Its Applications to Materials*, edited by M. de Graef and Y. Zhu (Academic Press, San Diego, 2001).
9. J. Miltat, and A. Thiaville, in *Encyclopedia of Materials: Science and Technology*, edited by K.H.J. Buschow, R.W. Cahn, M.C. Flemings, B. Ilschner, E.J. Kramer, and S. Mahajan (Elsevier Science, Amsterdam, 2001).
10. D. Rugar, H.J. Mamin, P. Guethner, S.E. Lambert, J.E. Stern, I. McFadyen, and T. Yogi, J. Appl. Phys. **68**, 1169 (1990).
11. U. Hartmann, T. Goeddenhenrich, and C. J. Magn. Magn. Mater. **101**, 263 (1991).
12. S. Porthun, L. Abelmann, and J.C. Lodder, J. Magn. Magn. Mater. **182**, 238 (1998).
13. A. Hubert and R. Schaefer, *Magnetic Domains* (Springer, Berlin, 1998).
14. P. Gruetter, D. Rugar, H.J. Mamin, G. Castillo, S.E. Lambert, C.J. Lin, and R.M. Valletta, Appl. Phys. Lett. **57**, 1820 (1990).
15. P.F. Hopkins, J. Moreland, S.S. Malhotra, and S.H. Liou, J. Appl. Phys. **79**, 6448 (1996).

16. G. Meyer and N.M. Amer, Appl. Phys. Lett. **53**, 1045 (1988).
17. D. Rugar, H.J. Mamin, and P. Guethner, Appl. Phys. Lett. **55**, 2588 (1989).
18. K. Babcock, M. Dugas, S. Manalis, and V. Elings, Mat. Res. Soc. Symp. **355**, 311 (1995).
19. W. Rave, L. Belliard, M. Labrune, A. Thiaville, and J. Miltat, IEEE Trans. Magn. **30**, 4473 (1994).
20. T.R. Albrecht, P. Gruetter, D. Horne, and D. Rugar, J. Appl. Phys. **69**, 668 (1991).
21. M. Dreyer, R.D. Gomez, and I.D. Mayergoyz, IEEE Trans. Magn. **36**, 2975 (2000).
22. G. Lévêque, P. Girard, S. Belaidi, and G. Cohen Solal, Rev. Sci. Instrum **68**, 4137 (1997).
23. P. Gruetter, Y. Liu, and P. LeBlanc, Appl. Phys. Lett. **71**, 279 (1997).
24. R. Proksch, K. Babcock, and J. Cleveland, Appl. Phys. Lett. **74**, 419 (1999).
25. Y. Liu and P. Gruetter, J. Appl. Phys. **83**, 7333 (1998).
26. L. Belliard, Ph.D. thesis, Orsay University, 1997.
27. L. Belliard, A. Thiaville, S. Lemerle, A. Lagrange, J. Ferré, and J. Miltat, J. Appl. Phys. **81**, 3849 (1997).
28. H.J. Hug, B. Stiefel, A. Moser, I. Parashikov, A. Kliczmik, D. Lipp, H.J. Guentherodt, G. Bochi, D.I. Paul, and R. C. O'Handley, J. Appl. Phys. **79**, 5609 (1996).
29. A. Fernandez, P.J. Bedrossian, S.L. Baker, S.P. Vernon, and D.R. Kania, IEEE Trans. Magn. **32**, 4472 (1996).
30. S. Gider, J. Shi, D.D. Awschalom, P.F. Hopkins, K.L. Campman, A.C. Gossard, A.D. Kent, and S. von Molnar, Appl. Phys. Lett. **69**, 3269 (1996).
31. M. Lederman, S. Schultz, and M. Ozaki, Phys. Rev. Lett. **73**, 1986 (1994).
32. L. Belliard, J. Miltat, A. Thiaville, S. Dubois, J.L. Duvail, and L. Piraux, J. Magn. Magn. Mater. **190**, 1 (1998).
33. Y. Henry, K. Ounadjela, L. Piraux, S. Dubois, J.M. George, and J.L. Duvail, Eur. Phys. J. **B20**, 35 (2001).
34. R.D. Gomez, T.V. Luu, A.O. Pak, K.J. Kirk, and J.N. Chapman, J. Appl. Phys. **85**, 6163 (1999).
35. J.M. Garcia, A. Thiaville, and J. Miltat, J. Magn. Magn. Mater. **249**, 163 (2002).
36. H. Joisten, S. Lagnier, M.H. Vaudaine, L. Vieux-Rochaz, and J.L. Porteseil, J. Magn. Magn. Mater. **233**, 230 (2001).
37. T. Shinjo, T. Okuno, R. Hassdorf, K. Shigeto, and T. Ono, Science **289**, 930 (2000).
38. J. Ferré, in *Spin Dynamics in Confined Magnetic Structures I*, edited by B. Hillebrands and K. Ounadjela (Springer, Berlin, 2002).
39. V. Gehanno, Y. Samson, A. Marty, B. Gilles, and A. Chamberod, J. Magn. Magn. Mater. **172**, 26 (1997).
40. A. Hubert, W. Rave, and S.L. Tomlinson, phys. stat. sol. (b) **204**, 817 (1997).
41. T. Chang, M. Lagerquist, J.G. Zhu, J.H. Judy, P.B. Fischer, S.Y. Chou, IEEE Trans. Magn. **28**, 3138 (1992).
42. OOMMF is a public micromagnetic program developed at the NIST, USA, by M.J. Donahue and coworkers. It is available at http://www.math.nist.gov. We used version 1.2α2.
43. I.A. Beardsley, IEEE Trans. Magn. **25**, 671 (1989).
44. B. Vellekoop, L. Abelmann, S. Porthun, and C. Lodder, J. Magn. Magn. Mater. **190**, 148 (1998).
45. H.J. Mamin, D. Rugar, J.E. Stern, R.E. Fontana, and P. Kasiraj, Appl. Phys. Lett. **55**, 318 (1989).
46. S. McVitie, R.P. Ferrier, J. Scott, G.S. White, and A. Gallagher, J. Appl. Phys. **89**, 3656 (2001).
47. A. Thiaville, L. Belliard, D. Majer, E. Zeldov, and J. Miltat, J. Appl. Phys. **82**, 3182 (1997).

48. P.J.A. van Schendel, H.J. Hug, B. Stiefel, S. Martin, and H.J. Guentherodt, J. Appl. Phys. **88**, 435 (2000).
49. S.L. Tomlinson and E.W. Hill, J. Magn. Magn. Mater. **161**, 385 (1996).
50. J. Miltat, G. Albuquerque, and A. Thiaville, in *Magnetism and Synchrotron Radiation*, edited by E. Beaurepaire, F. Scheurer, G. Krill, and J.P. Kappler (Springer, Berlin, 2001).
51. S. Foss, R. Proksch, E.D. Dahlberg, B. Moskowitz, and B. Walsh, Appl. Phys. Lett. **69**, 3426 (1996).
52. W. Rave, E. Zueco, R. Schaefer, and A. Hubert, J. Magn. Magn. Mater. **177–181**, 1474 (1998).
53. J.J. Saenz, N. Garcia, and J.C. Slonczewski, Appl. Phys. Lett. **53**, 1449 (1988).
54. D. Tomas, Ph.D. thesis, Charles University, 1999.
55. G. Albuquerque, J. Miltat, and A. Thiaville, J. Appl. Phys. **8**9, 6719 (2001).
56. J. Miltat, L. Belliard, A. Thiaville, D. Tomas, and F. Alouges, contribution HA01 at the 7th Joint MMM-Intermag Conference, 1998 (unpublished).
57. J.M. Garcia, A. Thiaville, J. Miltat, K.J. Kirk, J.N. Chapman, and F. Alouges, Appl. Phys. Lett. **79**, 656 (2001).
58. J.M. Garcia, A. Thiaville, J. Miltat, K.J. Kirk, and J.N. Chapman, J. Magn. Magn. Mater. **242–245**, 1267 (2002).
59. R. Proksch, P. Neilson, S. Austvold, and J.J. Schmidt, Appl. Phys. Lett. **74**, 1308 (1999).
60. M.M. Midzor, P.E. Wigen, D. Pelekhov, W. Chen, P.C. Hammel, and M.L. Roukes, J. Appl. Phys. **87**, 6493 (2000).